New Journal of Physics
The open access journal at the forefront of physics

Deutsche Physikalische Gesellschaft DPG | IOP Institute of Physics

PAPER • OPEN ACCESS

Enhanced four-wave mixing from multi-resonant silicon dimer-hole membrane metasurfaces

To cite this article: Lei Xu *et al* 2022 *New J. Phys.* **24** 035002

View the article online for updates and enhancements.

You may also like

- Active optical metasurfaces: comprehensive review on physics, mechanisms, and prospective applications
Jingyi Yang, Sudip Gurung, Subhajit Bej et al.

- Metasurfaces: a new look at Maxwell's equations and new ways to control light
M A Remnev and V V Klimov

- Resonant dielectric metasurfaces: active tuning and nonlinear effects
Chengjun Zou, Jürgen Sautter, Frank Setzpfandt et al.

This content was downloaded from IP address 58.6.169.69 on 01/08/2023 at 02:11

IOP Publishing | New J. Phys. 24 (2022) 035002 | https://doi.org/10.1088/1367-2630/ac55b2

New Journal of Physics
The open access journal at the forefront of physics

Deutsche Physikalische Gesellschaft DPG
IOP Institute of Physics

Published in partnership with: Deutsche Physikalische Gesellschaft and the Institute of Physics

CrossMark

OPEN ACCESS

RECEIVED
17 November 2021

REVISED
31 January 2022

ACCEPTED FOR PUBLICATION
16 February 2022

PUBLISHED
11 March 2022

Original content from this work may be used under the terms of the Creative Commons Attribution 4.0 licence.

Any further distribution of this work must maintain attribution to the author(s) and the title of the work, journal citation and DOI.

PAPER

Enhanced four-wave mixing from multi-resonant silicon dimer-hole membrane metasurfaces

Lei Xu[1,*], Daria A Smirnova[2,3], Rocio Camacho-Morales[2], Rifat Ahmmed Aoni[2], Khosro Zangeneh Kamali[2], Marcus Cai[2], Cuifeng Ying[1], Ze Zheng[1], Andrey E Miroshnichenko[4], Dragomir N Neshev[2] and Mohsen Rahmani[1,*]

1 Advanced Optics and Photonics Laboratory, Department of Engineering, School of Science and Technology, Nottingham Trent University, Nottingham NG11 8NS, United Kingdom
2 ARC Centre of Excellence for Transformative Meta-Optical Systems (TMOS), Research School of Physics, The Australian National University, Canberra, ACT 2601, Australia
3 Institute of Applied Physics, Russian Academy of Sciences, Nizhny Novgorod 603950, Russia
4 School of Engineering and Information Technology, University of New South Wales, Canberra ACT 2600, Australia
* Authors to whom any correspondence should be addressed.

E-mail: lei.xu@ntu.ac.uk and mohsen.rahmani@ntu.ac.uk

Keywords: metasurfaces, Mie resonances, bound state in the continuum, four wave mixing

Supplementary material for this article is available online

Abstract

Tailoring optically resonant features in dielectric metasurfaces unveils a robust scheme to control electromagnetic near fields of light and thus to boost the nanoscale nonlinear light–matter interactions. Membrane metasurfaces offer unique possibilities for supporting multipolar resonances and meanwhile maintaining high mode volume for enhancing nonlinear frequency conversion. Here we design a silicon membrane metasurface consisting of dimer airy holes, as a versatile platform for generating four-wave mixing (FWM). We show that such a metasurface exhibits a multi-resonant feature, including a quasi bound state in the continuum (BIC) generated by the collective toroidal dipole mode excited in the designed subdiffractive periodic system. We show that via employing the BIC mode in the short-wave infrared (SWIR), together with other resonant enhanced electric near fields in the near-infrared (NIR) region, simultaneously, one can convert invisible SWIR light to visible light radiation with high efficiency, via FWM. We experimentally demonstrated a significant FWM emission enhancement from our metasurface, which leads to a conversion efficiency of 0.76×10^{-6} using pump and signal beam peak intensities as low as 0.33 GW cm^{-2} and 0.17 GW cm^{-2}, respectively. Our results open new routes for enhancing nonlinear efficiencies for up-conversion processes.

1. Introduction

Optical nonlinear frequency conversion processes involve the interaction of two or more photons in a nonlinear medium to produce one or more photons at different frequencies. These processes form the basics for various nanophotonics applications including light sources [1–4], nanolasers [5–10], holograms [11], ultrafast all-optical light modulation [12–15], and bio-imaging applications [16]. In recent years, dielectric nanostructures have been introduced as promising nonlinear media for realising different functionalities thanks to their low losses at optical frequencies, as well as their multipole resonant nature [17–20]. The optical properties of dielectric nanostructures are governed by induced Mie-type electric and magnetic resonances. By exciting different multipolar resonances and through their interference in dielectric nanostructures, it allows efficiently shaping and manipulating light at the subwavelength scale. Trapping light in the dielectric nanostructures can offer bulk volume for light–matter interactions as compared to their nanoplasmonic counterparts where the confinement of electromagnetic fields of light occurs near the surface of nanoplasmonics. Besides, nanoplasmonics also suffer from material losses in the optical spectral

© 2022 The Author(s). Published by IOP Publishing Ltd on behalf of the Institute of Physics and Deutsche Physikalische Gesellschaft

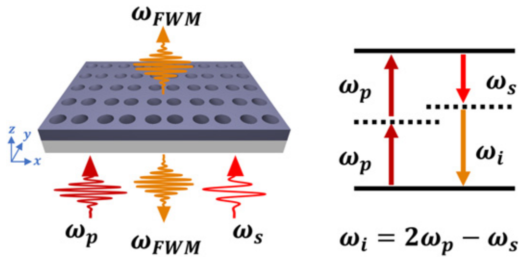

Figure 1. Schematic representation of the degenerate FWM process from our proposed amorphous Si dimer-hole membrane metasurface: a signal beam at SWIR frequency ω_s is mixed with a pump beam at NIR frequency ω_p to generate an idler output, which is the FWM radiation at frequency $\omega_i = 2\omega_p - \omega_s$.

region. Accordingly, dielectric nanostructures provide a powerful platform for boosting optical nonlinear frequency conversion [21–25, 25–28].

Four-wave mixing (FWM) is a third-order nonlinear effect where two or three different incident photons are mixed together to generate a new photon at a different frequency. The development of nanophotonics has served as an increasingly promising platform for enhancing the FWM process [29–38]. For the three-photon case, i.e. using three different frequencies as the input (ω_1, ω_2 and ω_3), a nondegenerate FWM process takes place and four different frequencies can be generated at $\omega_1 + \omega_2 + \omega_3$, $\omega_1 + \omega_2 - \omega_3$, $\omega_1 + \omega_3 - \omega_2$, and $\omega_2 + \omega_3 + \omega_1$. However, if the input consists of only two different frequencies, a degenerate FWM takes place and four different frequencies can be generated based on the equation $\omega_{\text{FWM}} = 2\omega_{1,2} \pm \omega_{2,1}$ [39]. It is worth mentioning that third-harmonic generation is a sub-category of FWM, where all the input photons possess the same frequency. In this paper, we study the case of two input photons in the near infra-red (NIR) and short-wave infrared (SWIR) spectral region, for enabling FWM process to generate light in the visible range (see figure 1). This configuration opens a promising pathway for enhancing nonlinear optical processes.

In the aforementioned cases, the nonlinear media is a key element for enhancing conversion efficiency. Recently, silicon metasurfaces, consisting of arrays of resonant silicon nanoparticles, have been introduced as a promising nonlinear media, due to their large linear refractive index and strong third-order nonlinearity, simultaneously. Besides, other advantages of a silicon platform are metal-oxide-semiconductor compatibility, low cost and well-established fabrication methods. Thus, silicon has been widely utilised to enhance the FWM processes [37, 40, 41].

Various resonant modes, generated by silicon metasurfaces, can facilitate trapping light and enhancing the nonlinear processes. Indeed, the possibility to arrange nanoparticles arbitrarily within a metasurface enables a combination of individual efficient resonances and the collective interactions between adjacent nanoantennas, which allows for achieving stronger optical responses and improved efficiencies. Therefore, one can obtain an efficient local control on the electromagnetic fields of light at nanoscale. A variety of resonant modes supported by silicon nanostructures have been investigated, including magnetic dipole resonances [42], Fano resonances [12, 43, 44], anapole states [45, 46], bound states in the continuum [47–53].

Moreover, by taking advantage of symmetry properties of the periodic system within the metasurfaces, one can support various symmetry-protected bound states in the continuum (BICs) [54, 55]. By breaking the symmetry of the system which supports a symmetry-protected BIC, one can transform an ideal BIC into a quasi-BIC. This allows obtaining an energy exchange with the external modes, and manifests itself as a sharp Fano feature in the optical response spectrum, leading to a strong near-field enhancement to further boost optical nonlinear light–matter interactions.

Here, we design a multi-resonant membrane metasurface consisting of dimer airy holes arranged periodically on a silicon slab (figure 1). Such a metasurface can support a strong toroidal dipole (TD) resonance in the SWIR wavelength range around 1560 nm, and simultaneously shows a strong resonant feature in the NIR wavelength region around 840 nm. Furthermore, the membrane feature can maintain high mode volume for enhancing light–matter interactions inside the material. We consider the degenerate FWM process in our case, which can be described in the right inset of figure 1 where an FWM light at the frequency $\omega_{\text{FWM}} = 2\omega_p - \omega_s$ is generated when illuminating the sample with two beams at frequencies ω_p and ω_s which we name as the pump and signal beams, respectively. We investigated the generation of visible light radiation based on the degenerate FWM of an SWIR signal beam with a NIR pump beam. The presence of resonances at the pump and signal wavelengths can significantly enhance the electric energy inside the structure. We observed a strong FWM emission, which corresponded to an FWM conversion

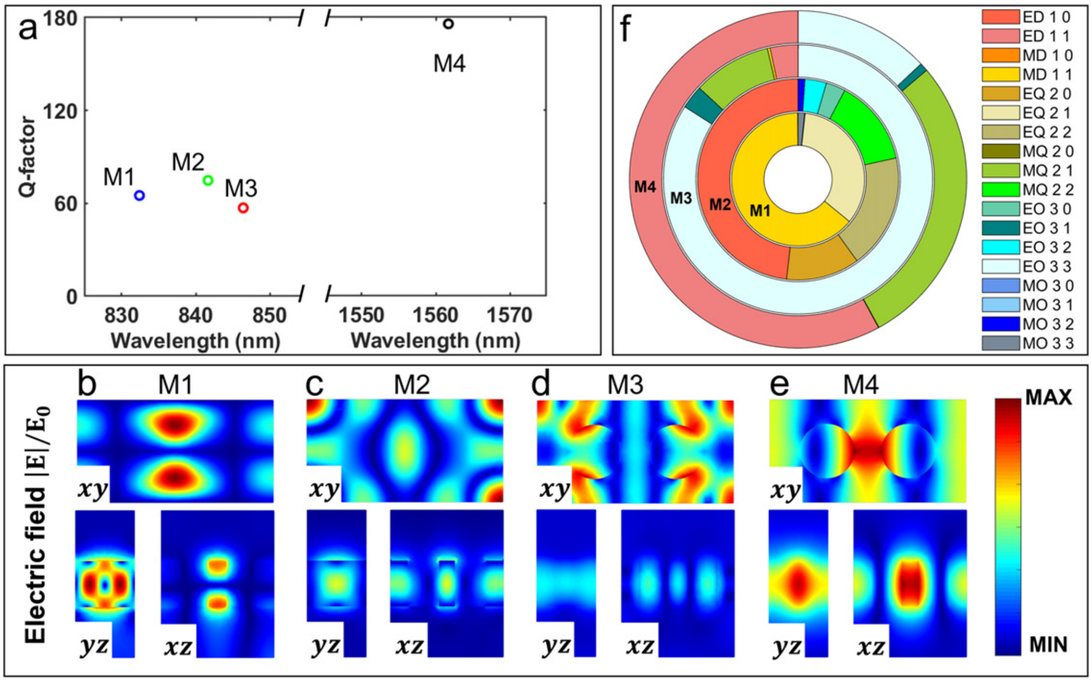

Figure 2. (a) Quality factors and wavelengths of the modes in the a-Si dimer-hole metasurface in the vicinity of the pump and signal wavelengths. (b)–(e) Electric near-field distributions for the modes M1 (b), M2 (c), M3 (d) and M4 (e), respectively. (f) Multipolar decompositions of the modes M1 to M4.

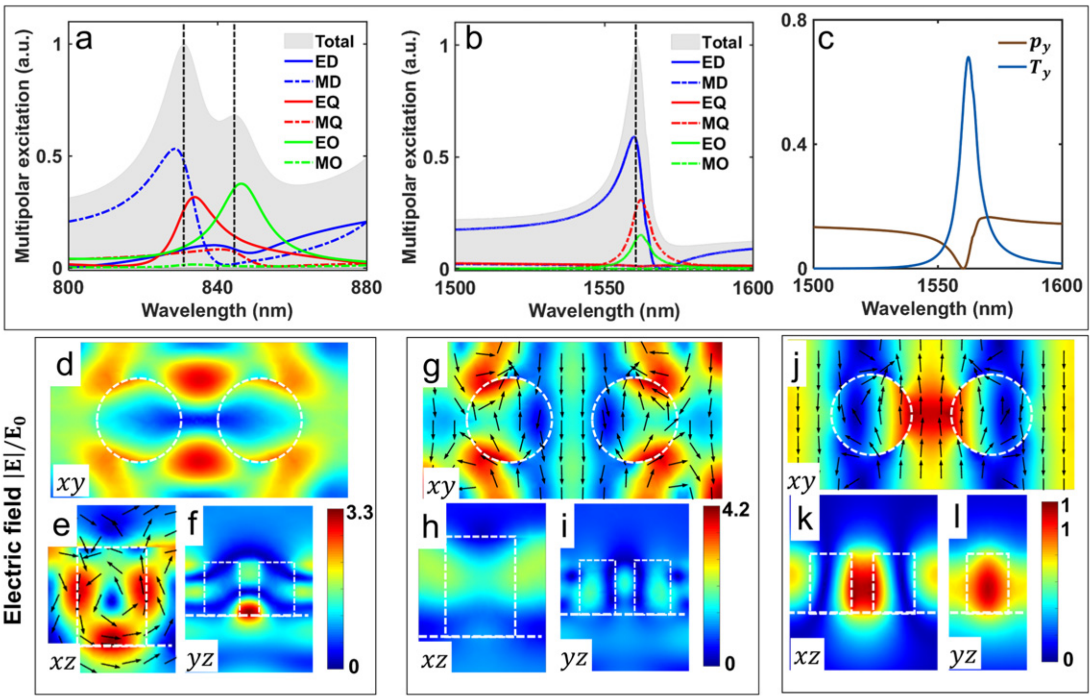

Figure 3. (a) Calculated spherical multipolar structure around the signal beam wavelength position. (b) Calculated Cartesian ED and TD modes excitations. (c) Calculated spherical multipolar structure around the pump beam wavelength position. (d)–(l) Electric near-field distributions at the resonant positions: (d)–(f) $\lambda_0 = 835$ nm. (g)–(i) $\lambda_0 = 846$ nm, (j)–(l) $\lambda_0 = 1565$ nm.

efficiency around 0.76×10^{-6} under a pump and signal beam peak intensities being 0.33 GW cm^{-2} and 0.17 GW cm^{-2}, respectively.

2. Results and discussions

In our study, we consider our pump beam wavelength λ_p around 840 nm, and our signal beam wavelength λ_s around 1565 nm. We aim to obtain large mode volume in the silicon material for enhancing the light–matter interactions and choose the membrane metasurface as our building blocks. We consider membrane metasurface consisting of a 235 nm-thick silicon slab with dimer airy holes arranged periodically on a glass substrate. The radius of the airy hole is fixed as $r_0 = 80$ nm, and the gap between the two airy holes (edge to edge) is set to be $g = 80$ nm. Both the signal and pump beams are y-polarised. To meet our requirements on the optical resonant responses in both SWIR and NIR wavelengths, we have investigated the transmission spectra from the metasurfaces with different pitch sizes D_x and D_y in x and y directions (see section 2 in the supplementary material (https://stacks.iop.org/NJP/24/035002/mmedia)). The pitch sizes D_x and D_y are optimised to be 575 nm and 300 nm respectively, to support strong resonant responses around the pump and signal wavelengths simultaneously. These resonant responses can be explained by the selective coupling of the incident plane wave light to different modes supported by the membrane metasurface. Figure 2(a) shows the numerically retrieved spectral position of the eigenmodes and their Q-factors around the pump and signal beam wavelengths. It is worth mentioning that in our case, the absorption of amorphous silicon material around pump wavelength is unavoidable. The real and imaginary part of the refractive index at the pump wavelength is measured to be 3.75 and 0.025, respectively. Figures 2(b)–(e) gives the calculated electric near-field spatial profiles accordingly. All these four modes exhibit large quality factors (more than 55) and can significantly enhance the electric near field in the silicon slab. These eigenmodes can be characterised by their multipolar structures over the spherical harmonics distinguished by the orbital index l and azimuthal index m [56, 57], as shown in figure 2(f). Mode M1 at 832 nm is dominated by strong in-plane magnetic dipole (MD) (with $m = \pm 1$) and electric duadrupole (EQ) (with $m = \pm 1$). Mode M2 at 842 nm is dominated by out-of-plane electric dipole (ED) (with $m = 0$), EQ (with $m = 0, \pm 2$), magnetic duadrupole (MQ) (with $m = \pm 2$), electric octupole (EO) (with $m = 0, \pm 2$) and magnetic octupole (MO) (with $m = \pm 2$), thus not having contribution of multipoles with $m = \pm 1$. Mode M3 at 846 nm is dominated by EO (with $m = \pm 1, \pm 3$), MQ (with $m = \pm 1$), ED (with $m = \pm 1$), and MD (with $m = \pm 1$). Mode M4 at 1561 nm is dominated by ED (with $m = \pm 1$), MQ (with $m = \pm 1$), and EO (with $m = \pm 1, \pm 3$). A y-polarised plane-wave contains multipoles exclusively with $m = \pm 1$ (see section 3 in the supplementary material). For the above-mentioned eigenmodes, only three of them (M1, M3 and M4) contain the multipoles with $m = \pm 1$, and can be excited directly under the y-polarised plane-wave beam incidence. However, for the eigenmode M2 (where the spectral position is in the vicinity of the pump beam) the coupling between the external plan-wave and the eigenmode M2 is forbidden as their multipolar structures do not share any multipole contents in common. This has also been verified from the calculated transmission spectra shown in section 2 of the supplementary material. Furthermore, the dependence of the resonance wavelengths on the periodicity can be described by the modified Fabry–Perot model for leaky mode TE(l_x, l_y, l_z) or TM(l_x, l_y, l_z) in resonant dielectric nanostructures [51, 58, 59]: $2\pi n_{\text{eff}} c/\lambda \sim (l_x - 1)\pi R_1 + (l_y - 1)\pi R_2 + (l_z - 1)\pi$. Here, l_x, l_y and l_z corresponds to the number of peaks of the electric/magnetic field within the domain along x, y and z directions. n_{eff} is the effective refractive index. The size ratio $R_1 = c/a$, $R_2 = c/b$. a, b and c are the size along x, y and z directions, which correspond to the periodicity D_x and D_y and the thickness of the slab h_0, respectively. For example, here M1 is a TM(3, 3, 1) leaky mode and M4 is a TE(3, 1, 1) leaky mode. Based on the above-mentioned formula, a linear dependence of the resonance wavelength for M4 on the pitch size p_x is expected: $\lambda \sim n_{\text{eff}} D_x$. While for M1, the resonance wavelength depends on both D_x and D_y: $\lambda \sim n_{\text{eff}} D_x D_y/(D_x + D_y)$.

We analyse the optical characteristics of our proposed membrane metasurface in the vicinity of the signal and pump wavelengths numerically by using the finite element method simulations in COMSOL. Figure 3(a) shows the calculated spherical multipolar structure of the membrane metasurface around the pump wavelength $\lambda_1 = 840$ nm under y-polarised plane wave illumination. A strong multipolar resonant feature is obtained around the pump wavelength range from 830 nm to 850 nm, which corresponds to the excitation of the eigenmodes M1 and M3, as illustrated in figure 2. The resonant response is dominated by the excitation of MD, EQ, and EO resonances with their peaks closely adjacent to each other. These strong multipolar resonant features further enable the efficient confinement of electric fields inside the silicon slab. Similarly, we have also performed the multipolar structure of the membrane metasurface around the signal wavelength λ_s under y-polarised plane wave illumination, as shown in figures 3(b) and (c). A strong resonant feature occurs around the spectral position of 1565 nm. The resonance is dominated by a Fano-shaped ED excitation with a strong contribution from the MQ and EO resonances. By further performing the Cartesian multipolar analysis as shown in figure 3(c), the excitation of ED is mainly contributed by a TD mode T_y with a strong electric field localised inside the silicon slab. This TD mode is

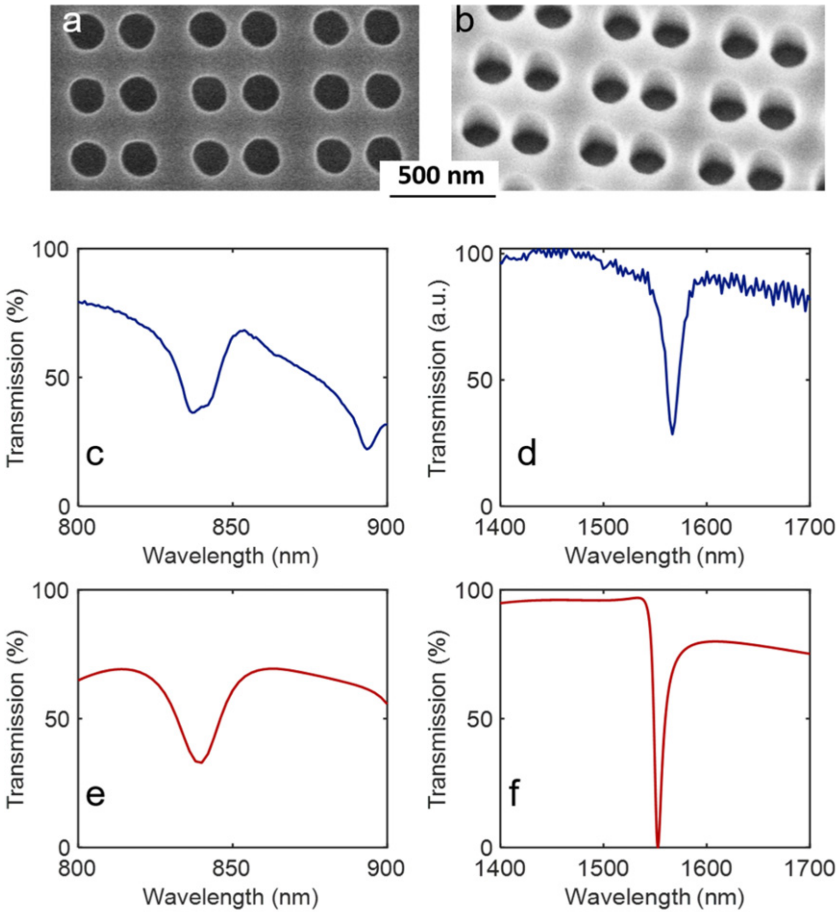

Figure 4. (a) and (b) SEM images of the fabricated sample showing the top view (a) and the side view with 40° tilt (b). (c) and (d) Experimentally measured linear transmission spectrum around (c) the pump beam wavelength position, and (d) the signal beam wavelength position. (e) and (f) Calculated linear transmission spectrum around (e) the pump beam wavelength position and (f) the signal beam wavelength position.

indeed a BIC that cannot be excited directly due to zero overlap between the mode profile and the outgoing waves, making it ideally uncoupled from the free-space radiation [47]. In our configuration, by adjusting the gap between the air holes, a 'bright' ED mode p_y (ED moment oriented along y direction) can be excited, playing a role in opening the leaky channel and transforming the ideal TD BIC mode into a quasi-BIC mode with a finite Q-factor. The spectral position of this TD BIC mode can be easily controlled by varying the pitch sizes D_x and D_y (as shown in the transmission spectra in section 2 of the supplementary material).

Figures 3(d)–(l) shows the electric near-field distributions for the wavelengths at the three resonant peak positions illustrated in figures 3(a) and (c). As can be seen, pronounced enhancements of the electric near-fields inside the silicon slab are obtained around both the signal and pump wavelengths, even in our case, the absorption of amorphous silicon is unavoidable at the pump wavelengths. By comparing the multipolar structure in figure 3 and the hierarchy of eigenmodes in figure 2, it clearly shows that the eigenmodes M1, M3, and M4 can be easily accessed and excited under the y-polarised pump and signal beam illuminations. These strong near-field enhancements hold promising potential for resonantly enhancing the nonlinear light–matter interactions by pumping photons at multiple resonant frequencies, and are ideal for the FWM process. In the following, we investigate the FWM process from the designed multi-resonant silicon membrane metasurface.

The nonlinear polarisation associated with the degenerated FWM process can be described in the following form [39]:

$$P_i(\omega_{\mathrm{FWM}}) = 3\epsilon_0 \sum_{jkl} \chi^{(3)}_{ijkl} E_j(\omega_{\mathrm{p}}) E_k(\omega_{\mathrm{p}}) E_l(\omega_{\mathrm{s}}^*), \tag{1}$$

where ϵ_0 is the vacuum permittivity. $\chi^{(3)}_{ijkl}$ is the third-order susceptibility tensor. $E_j(\omega_{\mathrm{p}})$, $E_l(\omega_{\mathrm{p}})$ are the jth and lth components of the electric field at the pump and signal frequencies ω_{p}, ω_{s}.

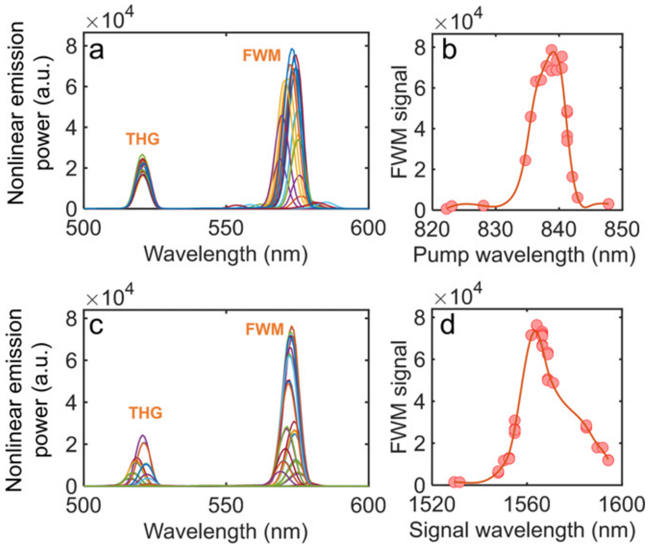

Figure 5. (a) Experimentally measured TH and FWM spectra under the excitation of different signal beam wavelengths (indicated by different colours). (b) The FWM emission power for different pump beam wavelengths. (c) Experimentally measured TH and FWM spectra under the excitation of different signal beam wavelengths (indicated by different colours). (d) The FWM emission power for different signal beam wavelengths.

For amorphous silicon, based on the intrinsic permutation symmetry, the $\chi^{(3)}_{ijkl}$ can be represented by

$$\chi^{(3)}_{ijkl} = \chi^{(3)}_{1122} \times (\delta_{ij}\delta_{kl} + \delta_{ik}\delta_{jl}) + \chi^{(3)}_{1221}(\delta_{il}\delta_{jk}). \tag{2}$$

Here, $\chi^{(3)}_{1122}$ and $\chi^{(3)}_{1221}$ are two elements of the third-order susceptibility tensor, and can be considered equal to each other for the amorphous silicon.

By introducing equation (2) to equation (1), we obtain the following form for the nonlinear polarisation [39, 40]:

$$\mathbf{P}_{\mathrm{FWM}}(\omega_{\mathrm{FWM}}) = 6\epsilon_0\chi^{(3)}_{1122}\left(\mathbf{E}(\omega_{\mathbf{p}})\cdot\mathbf{E}(\omega_{\mathbf{s}})^*\right)\mathbf{E}(\omega_{\mathbf{p}}) + 3\epsilon_0\chi^{(3)}_{1221}\left(\mathbf{E}(\omega_{\mathbf{p}})\cdot\mathbf{E}(\omega_{\mathbf{p}})\right)\mathbf{E}(\omega_{\mathbf{s}})^*. \tag{3}$$

Based on equation (3), by exciting resonances at pump and signal frequencies ω_{p}, ω_{s}, the electric fields of light $\mathbf{E}(\omega_{\mathrm{p}})$, $\mathbf{E}(\omega_{\mathrm{s}})$, can be highly confined inside the silicon nanostructures, leading to a strong near field enhancement that facilitate the generation of nonlinear polarisation of the FWM process.

We have fabricated our sample using the standard electron beam lithography. The membrane metasurface is fabricated out of the amorphous silicon on a glass substrate (see section 1 of the supplementary material). Figures 4(a) and (b) gives the scanning electron microscopy (SEM) images of the fabricated metasurface sample showing the top view and the side view (40° tilt), respectively. We measure the linear transmission spectrum of our sample in the spectral range of 800–900 nm and 1400–1700 nm, which correspond to the spectral region of pump and signal beams respectively. The experimentally measured transmission spectra are shown in figures 4(c) and (d). The pronounced resonant feature can be observed around the desired spectral positions in the NIR and SWIR wavelength ranges, respectively. The measured line shape of the spectra agrees well with our simulated results shown in figures 4(e) and (f), as well as with the theoretical analysis and the above-mentioned calculated multipolar structures shown in figure 3, indicating the successful excitation of the designed resonances from our sample.

We then perform the FWM spectroscopy measurement. Two femtosecond laser beams as the pump and signal beam respectively, with 167 fs pulse width for the pump beam, 147 fs for the signal beam, and 80 MHz repetition rate was focused by an aspheric lens with a focal length of 5 cm to a beam waist of 25 μm. The polarisation of the pump was adjusted along the y axis to excite the designed TD BIC mode and was tuned in the wavelength range of 1520 to 1600 nm. The polarisation of the signal beam was also adjusted along the y axis to excite the designed multipolar resonant responses near the pump wavelength around 840 nm. The forward nonlinear signal is then collected by an objective lens with NA = 0.4 and coupled to a spectrometer (see figure S4 in section 4 of the supplementary material). The raw data of the nonlinear emission intensity from the spectrometer is shown in figure 5.

By fixing the wavelength of the signal beam at $\lambda_{\mathrm{s}} = 1565$ nm, we first investigate the nonlinear spectra with varying pump beam wavelength from 820 nm to 850 nm, as shown in figure 5(a). We plot the FWM emission as a function of the pump beam wavelength in figure 5(b). As can be seen, the trend shows a clear

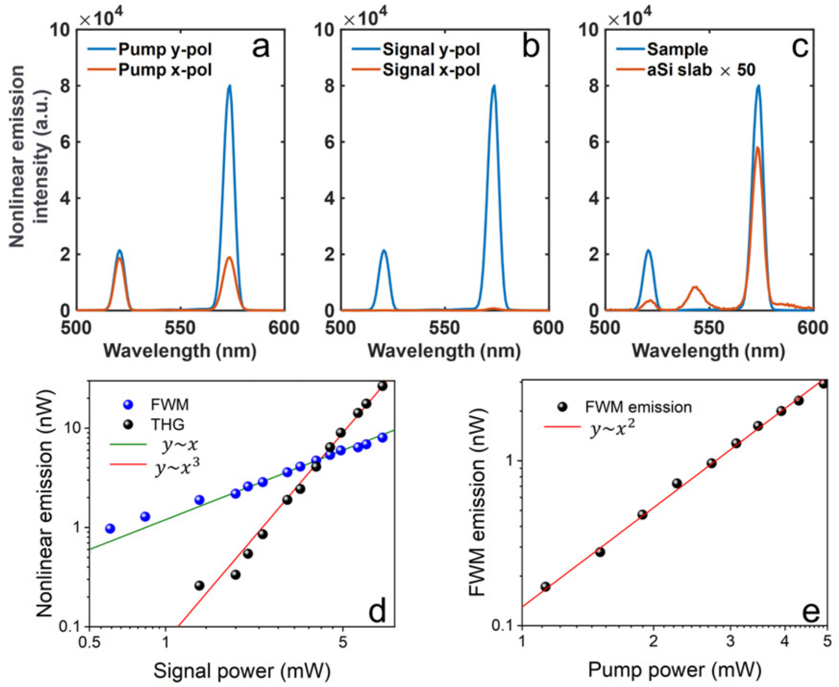

Figure 6. (a) The TH and FWM spectra under x- and y-polarised signal beam, respectively. (b) The TH and FWM spectra under x- and y-polarised pump beam, respectively. (c) The TH and FWM emission spectra of the designed sample and an aSi slab under y-polarised signal and pump beams illumination. (d) The experimentally measured intensity dependence of the FWM emission power in the forward direction on the pump beam power. (e) The experimentally measured intensity dependence of the FWM emission power and THG emission power in the forward direction on the signal beam power.

FWM emission enhancement when the pump beam wavelength is around 840 nm due to the strong resonant responses from the excited modes M1 and M3 at the pump beam (figure 3). On the other hand, when we fix the pump beam wavelength $\lambda_p = 842$ nm and tune the signal beam wavelength, due to the strong electric near-field enhancement at the TD BIC mode, we observe an FWM emission enhancement around $\lambda_s = 1565$ nm, as shown in figures 5(c) and (d). These measured nonlinear emission spectra match well with our theoretical analysis and the linear spectra (figures 3 and 4).

By fixing the pump and signal beams at the spectral positions of the resonances, i.e., $\lambda_p = 842$ nm $\lambda_s = 1565$ nm, we compare the FWM emission under different polarisation combinations of the pump and signal beams, as well as the FWM emission directly from the aSi slab, as shown in figures 6(a)–(c) which gives the raw data collected by the spectrometer. Our experimental results show that the FWM signal is significantly enhanced when both signal and pump beams are y-polarised, as compared to the cases when one of the beams is x-polarised. By comparing with the FWM emission directly from the aSi slab, the FWM emission from our designed dimer-hole membrane metasurface has been enhanced around 70 times. Furthermore, we observed a stronger enhancement of the THG emission ($3\omega_s$) from our sample: 200 times stronger than that from the silicon slab. This can be explained by the fact that for the THG process, the mode profiles of three fundamental photons are the same and completely overlap, while for FWM process, the overlap between the pump and signal beams depends on the excited modes, and they do not overlap completely. Meanwhile, our metasurface supports a stronger resonance and field confinement at the signal wavelength as there is negligible absorption from our experimentally obtained silicon material in the SWIR spectral range. We then study the power dependence of nonlinear emissions. By fixing the input power of the pump beam at 4.52 mW, we measured the TH and FWM emission power in the forward direction as a function of the input signal beam power, as shown in figure 6(d). As can be seen, a linear dependence of the FWM emission power to the signal beam power is obtained experimentally. This agrees well with the expectation from equation (3). For the THG process, we found the cubic dependence of the emission power to the signal beam power, as expected for a THG process based on the third-order nonlinearities of silicon material. Then, by fixing the power of the signal beam at 2.26 mW we obtain the dependence of FWM emission on the power of the pump beam, as shown in figure 6(e). As expected, we observe quadratic dependence of our FWM signal on the pump, which agrees well with equation (3). Here, the FWM conversion efficiency is defined as the ratio of the output idler power to the input signal power $\eta = P_{\mathrm{FWM}}/P_s$ [60], and it is estimated around 0.76×10^{-6} under a pump and signal beam peak intensity being 0.33 GW cm^{-2} and 0.17 GW cm^{-2}, respectively. We define the normalised FWM efficiency as

$\eta_{\mathrm{FWM}} = P_{\mathrm{FWM}}/(P_{\mathrm{p}}^2 P_{\mathrm{s}})$ which sorts out the dependence on the pump power level during the FWM process. In such a case, our designed membrane metasurface shows a normalised FWM conversion efficiency $\sim$2.4% W^{-2}.

3. Conclusion

In conclusion, we have demonstrated highly-efficient FWM from a silicon dimer-hole membrane metasurface with double resonances. The proposed membrane metasurfaces support a strong quasi-BIC TD mode around at the signal beam wavelength, and simultaneously it enables strong electric near-field enhancement due to the multipolar responses from MD, EQ, and EO at the pump beam wavelength. Such a multipolar resonant metasurface can significantly boost the nonlinear FWM process. Accordingly, we experimentally obtain a pump/signal-dependent FWM conversion efficiency around 0.76×10^{-6} under a pump and signal beam peak intensity being 0.33 GW cm^{-2} and 0.17 GW cm^{-2}, respectively. Importantly, by taking advantage of the quadratic dependence of the FWM emission power on the pump beam power, we can enhance the conversion of NIR light to visible radiation by tuning the pump beam power. Our results suggest a new paradigm for realising efficient nonlinear photonics metadevices.

Acknowledgments

LX and MR acknowledge support from the UK Research and Innovation Future Leaders Fellowship (MR/T040513/1). LX, MR and CY acknowledge the support from the Quality Research (QR) funding at NTU. The authors acknowledge funding support by the Australian Research Council (ARC) through Discovery Projects (DP200101353), Linkage Projects (LP180100904) and the Centre of Excellence program (CE200100010). DAS acknowledges financial support from the ARC Discovery Early Career Researcher Award (DE19010043) and the Russian Foundation for Basic Research (Grant No. 19-52-12053). Numerical modeling performed by DAS was partially supported by the Russian Science Foundation (Grant No. 20-72-00148). Rocio Camacho-Morales acknowledges a Grant from the Consejo Nacional de Ciencia y Tecnología (CONACYT), Mexico. ZZ acknowledges the support from the Royal Society scholarship. LX thanks Lujun Huang for valuable discussions. The authors acknowledge the use of Australian National Fabrication Facility (ANFF), the ACT Node, and NTU High Performance Computing cluster Hamilton.

Data availability statement

The data that support the findings of this study are available upon reasonable request from the authors.

ORCID iDs

Lei Xu https://orcid.org/0000-0001-9071-4311
Daria A Smirnova https://orcid.org/0000-0001-8033-3427
Rocio Camacho-Morales https://orcid.org/0000-0002-6102-7157
Rifat Ahmmed Aoni https://orcid.org/0000-0001-6310-0082
Khosro Zangeneh Kamali https://orcid.org/0000-0002-3160-737X
Marcus Cai https://orcid.org/0000-0002-0882-152X
Cuifeng Ying https://orcid.org/0000-0002-7279-1388
Ze Zheng https://orcid.org/0000-0002-9676-2856
Andrey E Miroshnichenko https://orcid.org/0000-0001-9607-6621
Dragomir N Neshev https://orcid.org/0000-0002-4508-8646
Mohsen Rahmani https://orcid.org/0000-0001-9268-4793

References

[1] Stav T, Faerman A, Maguid E, Oren D, Kleiner V, Hasman E and Segev M 2018 Quantum entanglement of the spin and orbital angular momentum of photons using metamaterials *Science* **361** 1101–4
[2] Wang K *et al* 2018 Quantum metasurface for multiphoton interference and state reconstruction *Science* **361** 1104–8
[3] Marino G *et al* 2019 Spontaneous photon-pair generation from a dielectric nanoantenna *Optica* **6** 1416–22
[4] Santiago-Cruz T *et al* 2021 Photon pairs from resonant metasurfaces *Nano Lett.* **21** 4423–9
[5] Noginov M A *et al* 2009 Demonstration of a spaser-based nanolaser *Nature* **460** 1110

[6] Totero Gongora J S, Miroshnichenko A E, Kivshar Y S and Fratalocchi A 2017 Anapole nanolasers for mode-locking and ultrafast pulse generation *Nat. Commun.* **8** 15535
[7] Ha S T, Fu Y H, Emani N K, Pan Z, Bakker R M, Paniagua-Domínguez R and Kuznetsov A I 2018 Directional lasing in resonant semiconductor nanoantenna arrays *Nat. Nanotechnol.* **13** 1042–7
[8] Lin Y, Wang D, Hu J, Liu J, Wang W, Guan J, Schaller R D and Odom T W 2019 Engineering symmetry-breaking nanocrescent arrays for nanolasing *Adv. Funct. Mater.* **29** 1904157
[9] Smirnova D *et al* 2020 Room-temperature lasing from nanophotonic topological cavities *Light Sci. Appl.* **9** 127
[10] Mylnikov V, Ha S T, Pan Z, Valuckas V, Paniagua-Domínguez R, Demir H V and Kuznetsov A I 2020 Lasing action in single subwavelength particles supporting supercavity modes *ACS Nano* **14** 7338–46
[11] Gao H, Fan X, Xiong W and Hong M 2021 Recent advances in optical dynamic meta-holography *Opto Electron. Adv.* **4** 210030
[12] Yang Y, Wang W, Boulesbaa A, Kravchenko I I, Briggs D P, Puretzky A, Geohegan D and Valentine J 2015 Nonlinear fano-resonant dielectric metasurfaces *Nano Lett.* **15** 7388–93
[13] Shcherbakov M R *et al* 2017 Ultrafast all-optical tuning of direct-gap semiconductor metasurfaces *Nat. Commun.* **8** 17
[14] Grinblat G, Berté R, Nielsen M P, Li Y, Oulton R F and Maier S A 2018 Sub-20 fs all-optical switching in a single Au-clad Si nanodisk *Nano Lett.* **18** 7896–900
[15] Grinblat G *et al* 2020 Efficient ultrafast all-optical modulation in a nonlinear crystalline gallium phosphide nanodisk at the anapole excitation *Sci. Adv.* **6** eabb3123
[16] Zhang S, Liu L, Ren S, Li Z, Zhao Y, Yang Z, Hu R and Qu J 2020 Recent advances in nonlinear optics for bio-imaging applications *Opto Electron. Adv.* **3** 10200003
[17] Kuznetsov A I, Miroshnichenko A E, Brongersma M L, Kivshar Y S and Luk'yanchuk B 2016 Optically resonant dielectric nanostructures *Science* **354** aag2472
[18] Neshev D and Aharonovich I 2018 Optical metasurfaces: new generation building blocks for multi-functional optics *Light Sci. Appl.* **7** 58
[19] Nemati A, Wang Q, Hong M and Teng J 2018 Tunable and reconfigurable metasurfaces and metadevices *Opto Electron. Adv.* **1** 180009
[20] Yang Q *et al* 2020 Mie-resonant membrane Huygens' metasurfaces *Adv. Funct. Mater.* **30** 1906851
[21] Smirnova D and Kivshar Y S 2016 Multipolar nonlinear nanophotonics *Optica* **3** 1241
[22] Rahmani M *et al* 2018 Nonlinear frequency conversion in optical nanoantennas and metasurfaces: materials evolution and fabrication *Opto Electron. Adv.* **1** 180021
[23] Krasnok A, Tymchenko M and Alù A 2018 Nonlinear metasurfaces: a paradigm shift in nonlinear optics *Mater. Today* **21** 8–21
[24] Chen S, Rahmani M, Li K F, Miroshnichenko A, Zentgraf T, Li G, Neshev D and Zhang S 2018 Third harmonic generation enhanced by multipolar interference in complementary silicon metasurfaces *ACS Photon.* **5** 1671–5
[25] Sain B, Meier C and Zentgraf T 2019 Nonlinear optics in all-dielectric nanoantennas and metasurfaces: a review *Adv. Photon.* **1** 024002
[26] Carletti L, Gandolfi M, Rocco D, Tognazzi A, de Ceglia D, Vincenti M A and De Angelis C 2021 Reconfigurable nonlinear response of dielectric and semiconductor metasurfaces *Nanophotonics* **10** 4209–21
[27] Pogna E A A *et al* 2021 Ultrafast, all optically reconfigurable, nonlinear nanoantenna *ACS Nano* **15** 11150–7
[28] Camacho-Morales R *et al* 2021 Infrared upconversion imaging in nonlinear metasurfaces *Adv. Photon.* **3** 036002
[29] Renger J, Quidant R, van Hulst N and Novotny L 2010 Surface-enhanced nonlinear four-wave mixing *Phys. Rev. Lett.* **104** 046803
[30] Wang Y, Lin C-Y, Nikolaenko A, Raghunathan V and Potma E O 2011 Four-wave mixing microscopy of nanostructures *Adv. Opt. Photon.* **3** 1–52
[31] Palomba S, Zhang S, Park Y, Bartal G, Yin X and Zhang X 2012 Optical negative refraction by four-wave mixing in thin metallic nanostructures *Nat. Mater.* **11** 34–8
[32] Zhang Y, Wen F, Zhen Y-R, Nordlander P and Halas N J 2013 Coherent Fano resonances in a plasmonic nanocluster enhance optical four-wave mixing *Proc. Natl Acad. Sci. USA* **110** 9215–9
[33] Cox J D and Javier García de Abajo F 2015 Plasmon-enhanced nonlinear wave mixing in nanostructured graphene *ACS Photon.* **2** 306–12
[34] Kravtsov V, Ulbricht R, Atkin J M and Raschke M B 2016 Plasmonic nanofocused four-wave mixing for femtosecond near-field imaging *Nat. Nanotechnol.* **11** 459–64
[35] Blechman Y, Almeida E, Sain B and Prior Y 2018 Optimizing the nonlinear optical response of plasmonic metasurfaces *Nano Lett.* **19** 261–8
[36] Rim W-S and Kim K-H 2019 Broadband visible-near infrared and deep ultraviolet generation by four-wave mixing and high-order stimulated Raman scattering from the hybrid metasurfaces of plasmonic nanoantennae and Raman-active nanoparticles *Phys. Chem. Chem. Phys.* **21** 26615–20
[37] Grinblat G, Li Y, Nielsen M P, Oulton R F and Maier S A 2017 Degenerate four-wave mixing in a multiresonant germanium nanodisk *ACS Photon.* **4** 2144–9
[38] Dai Y, Wang Y, Das S, Li S, Xue H, Mohsen A and Sun Z 2021 Broadband plasmon-enhanced four-wave mixing in monolayer MoS_2 *Nano Lett.* **21** 6321–7
[39] Boyd R W 2003 *Nonlinear Optics* (New York: Academic)
[40] Colom R *et al* 2019 Enhanced four-wave mixing in doubly resonant Si nanoresonators *ACS Photon.* **6** 1295–301
[41] Carletti L, Kruk S S, Bogdanov A A, De Angelis C and Kivshar Y 2019 High-harmonic generation at the nanoscale boosted by bound states in the continuum *Phys. Rev. Res.* **1** 023016
[42] Shcherbakov M R *et al* 2014 Enhanced third-harmonic generation in silicon nanoparticles driven by magnetic response *Nano Lett.* **14** 6488–92
[43] Shorokhov A S *et al* 2016 Multifold enhancement of third-harmonic generation in dielectric nanoparticles driven by magnetic Fano resonances *Nano Lett.* **16** 4857–61
[44] Xu L *et al* 2020 Enhanced light–matter interactions in dielectric nanostructures via machine-learning approach *Adv. Photon.* **2** 026003
[45] Shibanuma T, Grinblat G, Albella P and Maier S A 2017 Efficient third harmonic generation from metal-dielectric hybrid nanoantennas *Nano Lett.* **17** 2647–51
[46] Xu L *et al* 2018 Boosting third-harmonic generation by a mirror-enhanced anapole resonator *Light Sci. Appl.* **7** 44
[47] He Y, Guo G, Feng T, Xu Y and Miroshnichenko A E 2018 Toroidal dipole bound states in the continuum *Phys. Rev.* B **98** 161112
[48] Xu L *et al* 2019 Dynamic nonlinear image tuning through magnetic dipole quasi-BIC ultrathin resonators *Adv. Sci.* **6** 1802119

[49] Koshelev K, Tang Y, Li K, Choi D-Y, Li G and Kivshar Y 2019 Nonlinear metasurfaces governed by bound states in the continuum *ACS Photon.* **6** 1639–44
[50] Liu Z, Xu Y, Lin Y, Xiang J, Feng T, Cao Q, Li J, Lan S and Liu J 2019 High-*Q* quasibound states in the continuum for nonlinear metasurfaces *Phys. Rev. Lett.* **123** 253901
[51] Huang L *et al* 2021 Pushing the limit of high-*Q* mode of a single dielectric nanocavity *Adv. Photon.* **3** 016004
[52] Zheng Z, Komar A, Kamali K Z, Noble J, Whichello L, Miroshnichenko A E, Rahmani M, Neshev D N and Xu L 2021 Planar narrow bandpass filter based on Si resonant metasurface *J. Appl. Phys.* **130** 053105
[53] Fang C *et al* 2021 High-*Q* resonances governed by the quasi-bound states in the continuum in all-dielectric metasurfaces *Opto Electron. Adv.* **4** 200030
[54] Hsu C W *et al* 2016 Bound states in the continuum *Nat. Rev. Mater.* **1** 1–13
[55] Azzam S I and Kildishev A V 2021 Photonic bound states in the continuum: from basics to applications *Adv. Opt. Mater.* **9** 2001469
[56] Grahn P, Shevchenko A and Kaivola M 2012 Electromagnetic multipole theory for optical nanomaterials *New J. Phys.* **14** 093033
[57] Kroychuk M K, Shorokhov A S, Yagudin D F, Shilkin D A, Smirnova D A, Volkovskaya I, Shcherbakov M R, Shvets G and Fedyanin A A 2020 Enhanced nonlinear light generation in oligomers of silicon nanoparticles under vector beam illumination *Nano Lett.* **20** 3471–7
[58] Huang L, Yu Y and Cao L 2013 General modal properties of optical resonances in subwavelength nonspherical dielectric structures *Nano Lett.* **13** 3559–65
[59] Huang L *et al* 2016 Atomically thin MoS_2 narrowband and broadband light superabsorbers *ACS Nano* **10** 7493–9
[60] Foster M A, Turner A C, Sharping J E, Schmidt B S, Lipson M and Gaeta A L 2006 Broad-band optical parametric gain on a silicon photonic chip *Nature* **441** 960–3